Design of Sol–Gel Hybrid Bio-sourced Lignin/Silica Hydrophobic Nanocomposites through a Dip-Coated Evaporation-Induced Self-Assembly Method

Gabriel Cardoso Gonçalves, Florian Gimeno, Christophe Dicharry, Joachim Allouche, Fatima Charrier-El Bouhtoury, Jean-Charles Dupin

Design of sol-gel hybrid bio-sourced lignin/silica hydrophobic nanocomposite through a dip-coated Evaporation Induced Self-Assembly (EISA) method

Journal:	*ACS Sustainable Chemistry & Engineering*
Manuscript ID	sc-2022-03770a
Manuscript Type:	Article
Date Submitted by the Author:	24-Jun-2022
Complete List of Authors:	Cardoso Gonçalves, Gabriel; Université de Pau et des Pays de l'Adour, E2S IPREM CNRS UMR 5254 Gimeno, Florian; Université de Pau et des Pays de l'Adour, E2S IPREM UMR 5254 CNRS Dicharry, Christophe; Université de Pau et des Pays de l'Adour, Laboratoire des Fluides Complexes et leurs Réservoirs-IPRA, UMR5150 Allouche, Joachim; Université de Pau et des Pays de l'Adour, CNRS/ Univ Pau & Pays Adour/ E2S UPPA, Institut des Sciences Analytiques et de Physicochimie pour l'Environnement et les Matériaux, UMR 5254 Charrier - El Bouhtoury, Fatima; Universite de Pau et des Pays de l\'Adour UFR des Sciences et Techniques, Sciences et technologies Dupin, Jean-Charles; Université de Pau et des Pays de l'Adour, E2S IPREM UMR CNRS 5254

Design of sol-gel hybrid bio-sourced lignin/silica hydrophobic nanocomposite through a dip-coated Evaporation Induced Self-Assembly (EISA) method

*Gabriel Cardoso Gonçalves†, Florian Gimeno†, Christophe Dicharry†, Joachim Allouche†, Fatima Charrier-El Bouhtoury ‡ and Jean-Charles Dupin†**

† Université de Pau et Pays de l'Adour, E2S UPPA, IPREM/CNRS, UMR5254, 64000, Pau, France

‡ Université de Pau et Pays de l'Adour, E2S UPPA, IPREM/CNRS, UMR5254, 40000, Mont de Marsan, France

ABSTRACT

Lignin-silica hybrid nanocomposite films were prepared on aluminum alloys 2024 through a dip-coating process combined to an Evaporation Induced Self-assembly methodology using Kraft Lignin and Tetraethyl Orthosilicate (TEOS) as the organic and the inorganic sources respectively. Dip Coating parameters like withdrawal speed and relative humidity were optimized to create the best coating deposition. Two different synthesis pathways, direct (DR) and non-direct (NDR), were evaluated. The NDR synthesis involved a pre-coating functionalization of the substrate by a 3-(Triethoxysilyl) propylsuccinic alkoxysilane linker, which provides a significant improvement

and enhancement of the film stability due to the creation of anchorage sites for the hybrid composite. The surface morphology of the material, its chemical composition and wettability were analyzed by Scanning Electron Microscopy (SEM), Fourier Transform Infrared Spectroscopy (FTIR), X-Ray Photoelectron Spectroscopy (XPS) and Water Contact Angle Measurement (WCA). The results show a hydrophobic behavior of the hybrid film coating improved by the self-assembly of lignin nanoparticles on the surface.

KEYWORDS: Lignin, Evaporation Induced Self-Assembly (EISA), bio-sourced coating, hydrophobicity, XPS spectroscopy, Al 2024

Introduction

Aluminum alloys are a series of materials widely used in the aeronautical sector due to their good mechanical and low density properties. However, these alloys are submitted in condition of use to several deterioration processes including corrosion damages that has to be prevented by stable protection coatings[1]. For years, Chromate Conversion Coatings (CCC) based on the extremely toxic hexavalent Cr VI have been used and established as the principal protection for Al alloys. However, with the start of European REACH Legislation and the progressive interdiction of toxic and hazardous chemical compounds since 2007, new protection alternatives are being studied and developed to fit a more ecofriendly way and confirm the objective of REACH legislation to completely ban the CCC until 2024[2].

In this context, alternative coatings based on compounds like molybdenum, zirconium titanium among others[3] and afterwards bio-sourced materials**Erreur ! Source du renvoi introuvable.** have been evaluated as possible substitutes to CCC. In the latter case, lignin bio-sourced based materials have

recently been considered as good candidates due to their heat resistance, their good coating mechanical properties and the vast abundance of lignin[5].

The lignin is a complex biopolymer with a three-dimensional structure based on cross linked phenolic groups. In addition, its physico-chemical properties depend on the relative proportion of the main chemical groups: syringyl (S), guaiacyl (G) and p-hydroxyphenyl (H), which the proportions will define the final characteristics of the complex molecule[7] . As the second most abundant biopolymer on Earth after cellulose, lignin plays a key role in the structural constitution of the walls of wood, herbals and other plants conferring an important role of physical rigidity and facilitating the transport of water due to its hydrophobic character[8]. One of the most important industrial processes related to lignin extraction is the Kraft pulping, that is capable to separate the lignin from cellulose after processes using sodium hydroxide and sodium sulphite[9]. The final obtained lignin has a high molecular weight (more than 2000 g/mol), reveals the presence of residual sulfur (from the extraction process) and its structure is modified during the Kraft process, as β-ether bonds are break down creating an abundant quantity of C-C bonds[10].

The lignin extraction market was expected to reach a market size of around 611 million dollars in 2021[11], but despite the high economic amount, most of the lignin production is destined to be burned and used as an energy source. Only 2% of its total production are used for applications of greater scientific value as binders and nanoparticles fabrication. Thus, looking for new applications, first studies have been highlighted the promising implementation of lignin in bio-sourced materials, in which properties like high content of cross-linking and natural hydrophobicity can confer interesting wettability properties to final protective layers[12].

In such context of protective coating materials, several deposition techniques have been performed and optimized over the years to study and improve the interaction of lignin based

materials with different substrates. For instance, simple methods such as drop-casting of lignin solution on a substrate surface were studied by Lee and Luner[13], but it was proven that this methodology only based on controlling the process temperature and applied pressure on the film did not produce a stable material under the conditions of use. More versatile methods using deposition processes like spin coating[14], electrophoretic deposition[15] and dip-coating**Erreur ! Source du renvoi introuvable.** have also been explored using pristine or modified lignin into polymeric and metallic substrates. Such techniques lead to relatively stable coating layers and allow the development of organic-inorganic hybrid materials associating inorganic sources and lignin.

Considering these points, our work is focused on the development of a versatile way to produce a lignin-based hybrid coating on Al 2024 alloy substrate by dip-coating but using a substrate pre-functionalized step with the coupling agent 3-(Triethoxysilyl)propylsuccinic acid (TESPSA) prior to film deposition. To our knowledge, such strategy has not been explored previously on lignin base coating on metal substrate.

In this context, lignin-silica film nanocomposite on Al 2024 alloy has been prepared through a dip-coating process using an Evaporation Induced Solvent Self-Assembly (EISA) strategy. EISA is a powerful chemical method widely used to design well-defined hybrid nanostructured and nanopatterned materials[17]. Such technique based on organic and inorganic entities self-assembly leads to structuration at nanoscale of metal oxides using structuring organic mesophases from inorganic precursors in solution and triggered by the solvent evaporation. Combining such technique to a dip-coating process allows to optimize the structure and morphology of the hybrid coatings by controlling the experimental conditions like the withdrawal speed, the relative humidity or the deposition temperature[18]. We have taken advantage of the EISA methodology to prepare hybrid lignin/silica film nanocomposites through typical sol-gel process using two

synthetic pathways. One of them involves a substrate pre-coating functionalization step by TESPSA, an organo-alkoxide precursor able to create ester bonds that improves both the interaction between the coating layer and the substrate and the interconnection of the organic and inorganic networks within the hybrid materials. Particularly, the influence of such functionalization and the full characterization of the coatings were studied using a panel of techniques including X-Ray photoelectron spectroscopy (XPS), Fourier Transform Infrared Spectroscopy (FTIR), Scanning Electron Microscopy (SEM), Contact Angle measurements and roughness evaluation.

Materials and Methods

Chemicals and substrates

The used kraft lignin is a non-toxic product from renewable sources which was bought from UPM Biochemicals (UPM BiopivaTM 100) and no further modified (molecular weight Mw, 5000g/mol). Tetrahydrofuran (THF), Acetone 99.5%, Tetraethyl orthosilicate (TEOS) 98%, Hydrochloric Acid (HCl) 36%, Nitric Acid (HNO3) 65% and 3-(Triethoxysilyl)propylsuccinic anhydride (TESPSA) 95% were all provided by Merck, the Toluene 99.5% used was obtained at ACROS ORGANICS and the Sodium Hydroxide (NaOH) 97% at PROLABO.

The 300 mm x 300 mm x 1.60 mm dimensions aluminum alloy 2024-T3 plate (Al 93.5 wt% / Cu 4.5 wt% / Mg wt1.5% / Mn 0.5 wt% nominal composition) from Goodfellow Cambridge Ltd. was cut into 60 mm x 20 mm x 1.60 mm substrates before deposition.

Pre-coating chemical preparation of the substrates

The Al 2024 alloy surface was prepared before coating following a protocol insuring at the same time a subsequent increase of the roughness and the hydroxylation of the surface to facilitate the anchorage of the active hybrid layer.

The preparation started with the immersion under sonication of the Al alloy substrate in acetone for 10 minutes (room temperature) insuring the degreasing of the surface. Then, an alkaline pickling (NaOH 2.5 M) was done during 1 minute at 45°C and followed by an acid etching (HNO3 1.6 M) for 30 minutes at room temperature.

Solution preparation

Two solutions of lignin were prepared for the coatings. The first one (Solution A) is prepared by mixing the Kraft Lignin with TEOS as the silica source. This preparation method is adapted from a procedure according to the work of J. Wei et al.[19]. Typically, 0.12 g of Kraft Lignin was solubilized in 23.60 mL of THF and sonicated for 45 min. Then, the resulted brown solution was acidified with the addition of 5.83 mL of 2M HCl and 0.97 mL of TEOS were finally added. The solution was kept stirring and aging overnight to provide a complete TEOS hydrolysis. The final weight ratio of such Lignin/THF/HCl 2M/TEOS solution is 1/175/50/7.5 (molar ratio: $1/8.6\times10^{-5}/1.5\times10^{-4}/5.8\times10^{-3}$) respectively and has a measured viscosity of 1.5 mPa.s (Anton Paar MCR 302e Rheometer). The second solution (Solution B) is the same than the previous one but without any silica source and had a measured viscosity of 1.3 mPa.s. The whole preparation procedure is identical except the addition of TEOS.

Coatings and substrate functionalization

The coatings were prepared following a direct route (DR) and a non-direct route (NDR). The NDR procedure only differs from the DR pathway by a pre-functionalization step of the substrate before coating. Such functionalization consists in the grafting of 3-(triethoxysilyl)propylsuccinic

(TESPSA) on the aluminum alloy as an organo-alkoxide linker coupling molecule. Typically, the pre-functionalization of the surface was done by immersing the previously prepared Al 2024 substrate in a solution of TESPSA/Toluene 2% v/v at 60 °C overnight. Afterwards, the sample was washed with toluene and then immersed for 10 min in the same solvent at 100 °C to ensure the removal of weak bonds. Finally, the samples were dried under nitrogen flow for 1 minute[20].

For both the DR and the NDR routes, the coatings were carried out by a dip-coating process using an ACEdip 2.0 dip-coater model (SolGelWay, France). Either the solution A or solution B was used as the immersion bath. The conditions of deposition were optimized by the control of the parameters given in the Table 1. Particularly, due to the moderate viscosity and the precursor concentration of the solutions, a low relative humidity (RH) and a micronic withdrawal speed were chosen to speed up the evaporation process and to target the capillarity coating regime to increase the thickness of the material deposition[21].

Table 1. Dip-Coating constant parameters used for deposition.

Parameter	Value
Temperature	25.00 ± 2.00 °C
Withdrawal speed	0.05 mm/s
Immersion Speed	10.00 mm/s
Immersion Time	5 seconds
Number of Cycles	1
Relative Humidity	10%

After deposition, the samples were left to dry inside the dip-coater chamber for 3 minutes before finally thermally treated in an oven at 120°C for 5 minutes. For both, DR and NDR routes, the deposition parameters were identical.

X-Ray Photoelectron Spectroscopy (XPS)

XPS measurements for chemical analysis of samples were run with a Thermo K-alpha spectrometer working with a hemispherical analyzer and a micro focused (400 μm diameter microspot) monochromatic radiation (Al Kα, 1486.6 eV) operating at 72 W under a residual pressure of 1.10−9 mbar. Pass energy was adjusted to 20 eV. To compensate the charge effects present on the analysis, a dual beam charge neutralization system (low energy electrons and Ar+ ions), which has the unique ability to provide consistent charge compensation was used. For the quantification of the spectra, all Relative Sensitive Factors (R.S.F.) were imported from the Scofield cross sections database.

Three types of analysis were performed, a single surface point analysis using the parameters described above, a large area analysis ("chemical map") with a pass energy of 80 eV and a 20 μm step, for a total of 560 analyzed surface points and finally a depth profile, with an Ar+ ion beam at a 3000 eV energy. The sample was etched for 40 seconds/cycle, and a total of 60 cycles was performed.

The calibration of all spectra was based on the binding energy of aliphatic carbon considered at 285.0 eV. The mathematical fitting was done with the software Casa XPS using a least-squares algorithm and a non-linear baseline (Shirley). The experimental curves peaks were fitted using a combination of Gaussian (70%) and Lorentzian (30%) distributions.

The control of the natural aluminum oxide passive layer thickness (dAl2O3) on the metal substrate was done using the following equation[22]:

$$(\mathrm{d_{Al2O3}})(\mathrm{nm}) = \lambda_o osin\theta . sin\theta \left(\frac{N_m \lambda_m I_o}{N_o \lambda_o I_m} + 1\right)$$

Where Nm and No are the metal and oxide densities respectively (Nm =2.7 g/cm3 and No=3.95 g/cm3), λ is the inelastic mean free path (IMFP) calculated in[23] and reported as 26 nm for the Al metal and 28 nm for Al oxide. The oxide to metal peak ratio (Io/Im) was obtained from XPS quantification. The theta (θ) angle used was 54.7 degrees and depends on the inner optical configuration of the spectrometer.

Scanning Electron Microscopy (SEM)

All SEM images were recorded with a JEOL JAMP-9500F Field Emission dual Auger-SEM Microprobe equipment, operated at 30 kV and 5 nA. The analyzed samples were coated with a thin layer of gold generated from a DESK V (Denton Vacuum) metallizer for 1 minute at 50 mA.

Fourier Transform Infrared Spectroscopy (FTIR)

FTIR analysis were performed in a Nicolet Spectrometer model 6700 (Thermo Scientific) in ATR mode. All spectra were obtained in a range of 600 cm^{-1} to 4000 cm^{-1} in the transmittance mode, 64 scans were performed with a step of 2 cm^{-1} and resolution of 4 cm^{-1}. To acquire the results, the coatings were removed from the substrate by scraping and then analyzed.

Water Contact Angle measurements (WCA)

The WCA measurements were performed with a Tracker Automatic Drop tensiometer from Teclis Scientific. The volume of the water droplet was kept 3 µL for all measurements at 25°C and for an acquisition time of 5 minutes. The relative incertitude of the measures is ± 2°.

Roughness evaluation

The surface roughness was measured with a Micromesure CHR150 profilometer (STIL Society), providing 2D and 3D profiles. The profilometer is equipped with a high-resolution sensor that allows measurements in small units. The data was acquired in the SurfaceMap Software and then

the results treated by the software MountainsMap®Scanning Topography 7.4.9391, that provided the root main square height (Sq) following ISO 25178 standard.

Results and Discussion

Physico-chemical characterization of the Kraft Lignin

The Kraft Lignin powder was characterized before used in the materials preparation. The SEM images revealed a dense and big agglomerates structure (Figure 1a), made of particles with a micro globular morphology.

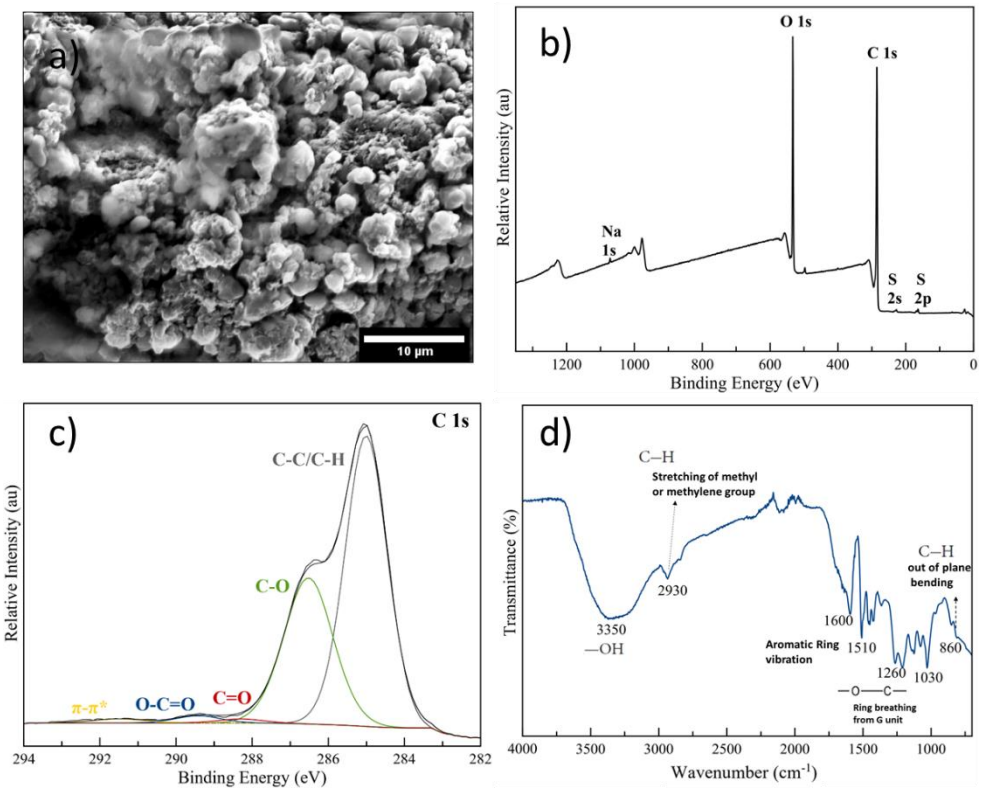

Figure 1. Physico-chemical characterization of the Kraft Lignin powder: SEM image (a), XPS general survey (b) and C 1s core level spectra (c) and FTIR spectrum (d).

XPS analyses were performed to obtain a better view of the chemical composition and signature of the raw material. In Figure 1b, the most intense peak of lignin general spectrum (around 284.9

eV) corresponds to C 1s orbital, and represents almost 80 at.% of the total composition (Table 2). The minor elements traces found, sulfur, nitrogen and sodium, are from the extraction process.

The associated C 1s spectrum, Figure 1c, confirms the complex chemical composition of the biopolymer, with four major different carbon chemical environments C-C/C-H, C-O, C=O, O-C=O. The C-C/C-H bonds (285.0 eV) in association with C-O (286.5 eV) constitutes almost 100 % of the total chemical environment, what is expected, once the molecular structure of the Lignin is mainly based on these interactions, as stated by Brazil T. et al.[24]. The component in 291.5 eV is related to π–π* transition.

Table 2. XPS quantitative data of Kraft Lignin.

Core Peak	Kraft Lignin		
	BE (eV)	at.%	Total At. Conc (%)
C 1s	285.0	47.4	77.9
	286.5	27.7	
	288.3	0.7	
	289.4	1.3	
	291.5	0.8	
O 1s	532.9	3.5	20.8
	534.2	17.3	
N 1s	401.0	0.1	0.1
Na 1s	1072.9	0.3	0.3
S 2p	164.5	0.4	0.9
	165.8	0.2	
	169.7	0.2	

	170.8	0.1

In good agreements with the previous XPS characterization, the FTIR analysis of the Lignin (Figure 1d) displays some characteristic bands related to the lignin molecular structure. The peaks around 1510 cm^{-1} and 1600 cm^{-1} are related to vibrations of aromatic groups. Around 1030 cm^{-1} a band from C-H bond stretching and the shoulder, at 1260 cm^{-1}, identifies the guaiacyl bond in lignin[25]. In addition, at higher wavenumbers around 3350 cm^{-1} an intense band from -OH stretching can be observed.

Aluminum substrate characterization after chemical pre-coating treatment

The characterization of the surface state of the alloy substrate in terms of morphology and chemical composition is of primary importance for the material deposition processes

understanding. SEM images revealed some differences between the raw Al 2024 substrate (

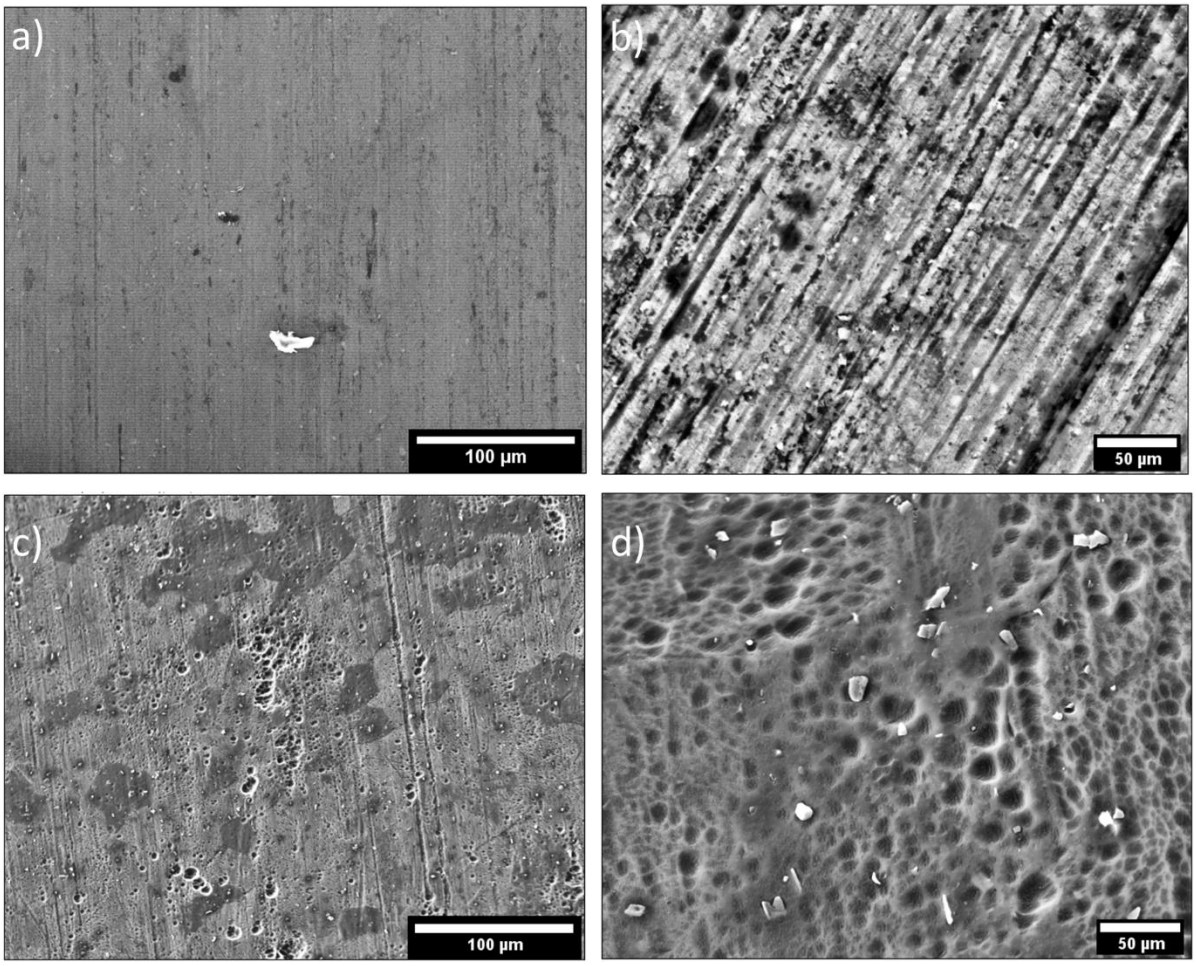

Figure **2**a), in which some machining scratches are visible (

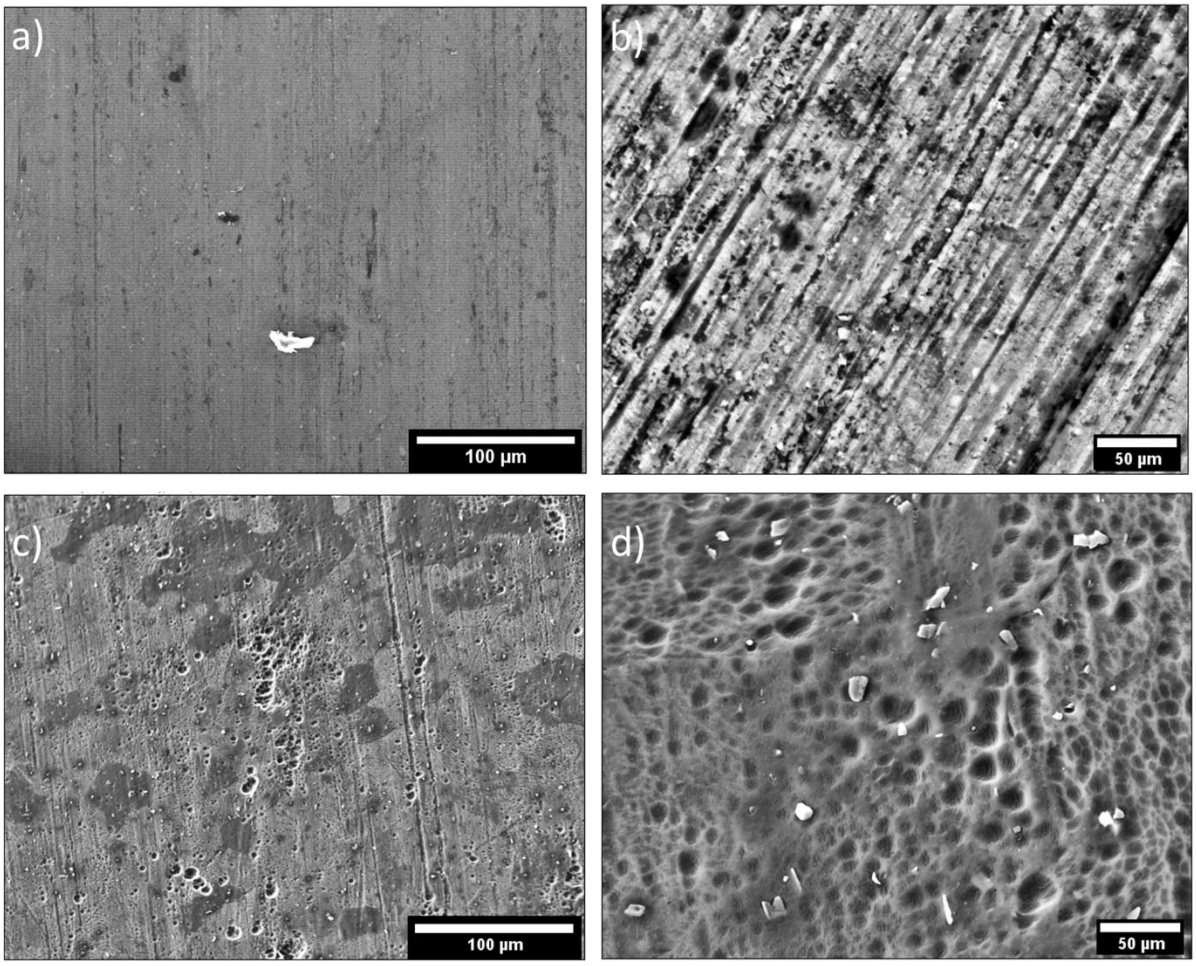

Figure **2**b) and the prepared substrate (

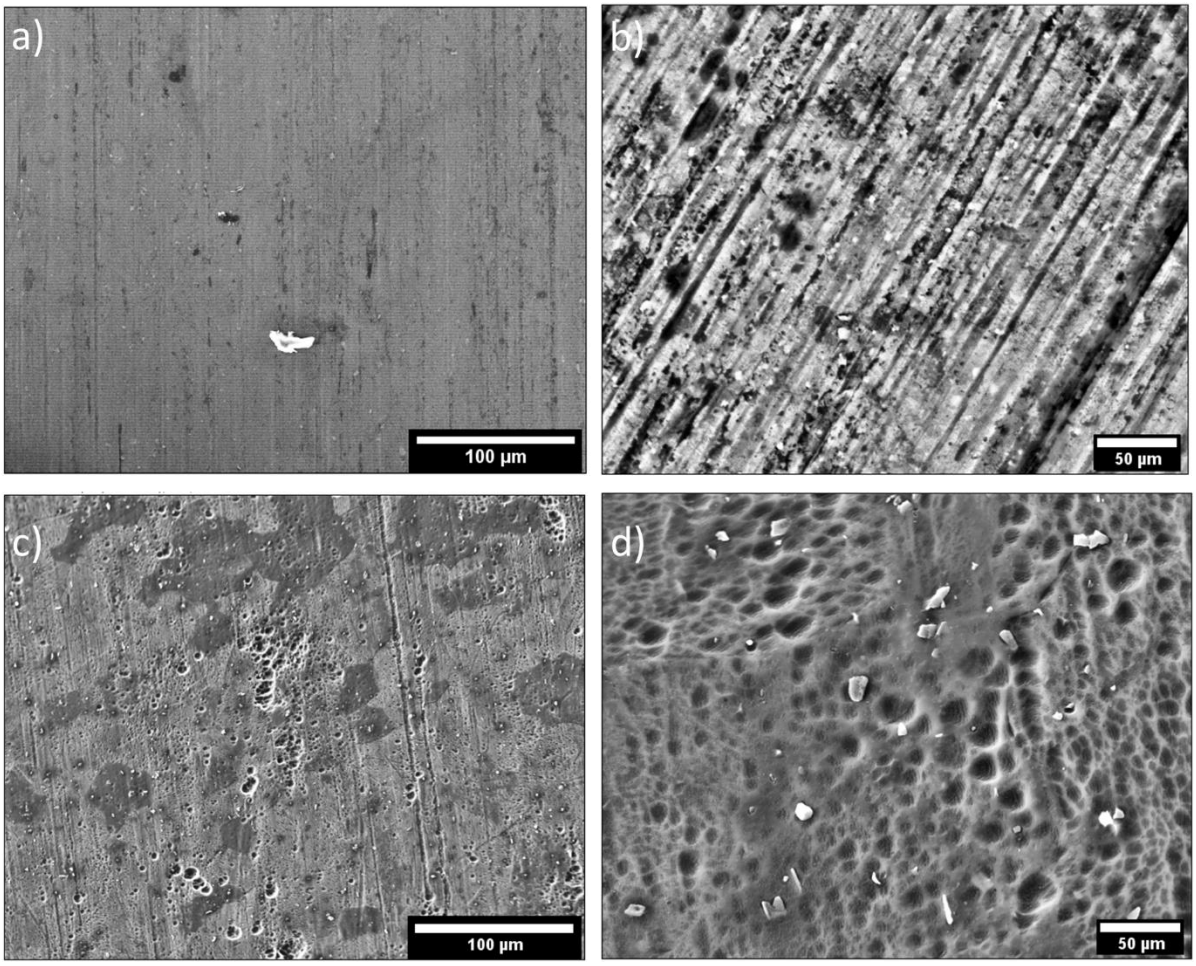

Figure **2**c) with some bright and white structures, stated as intermetallic particles (

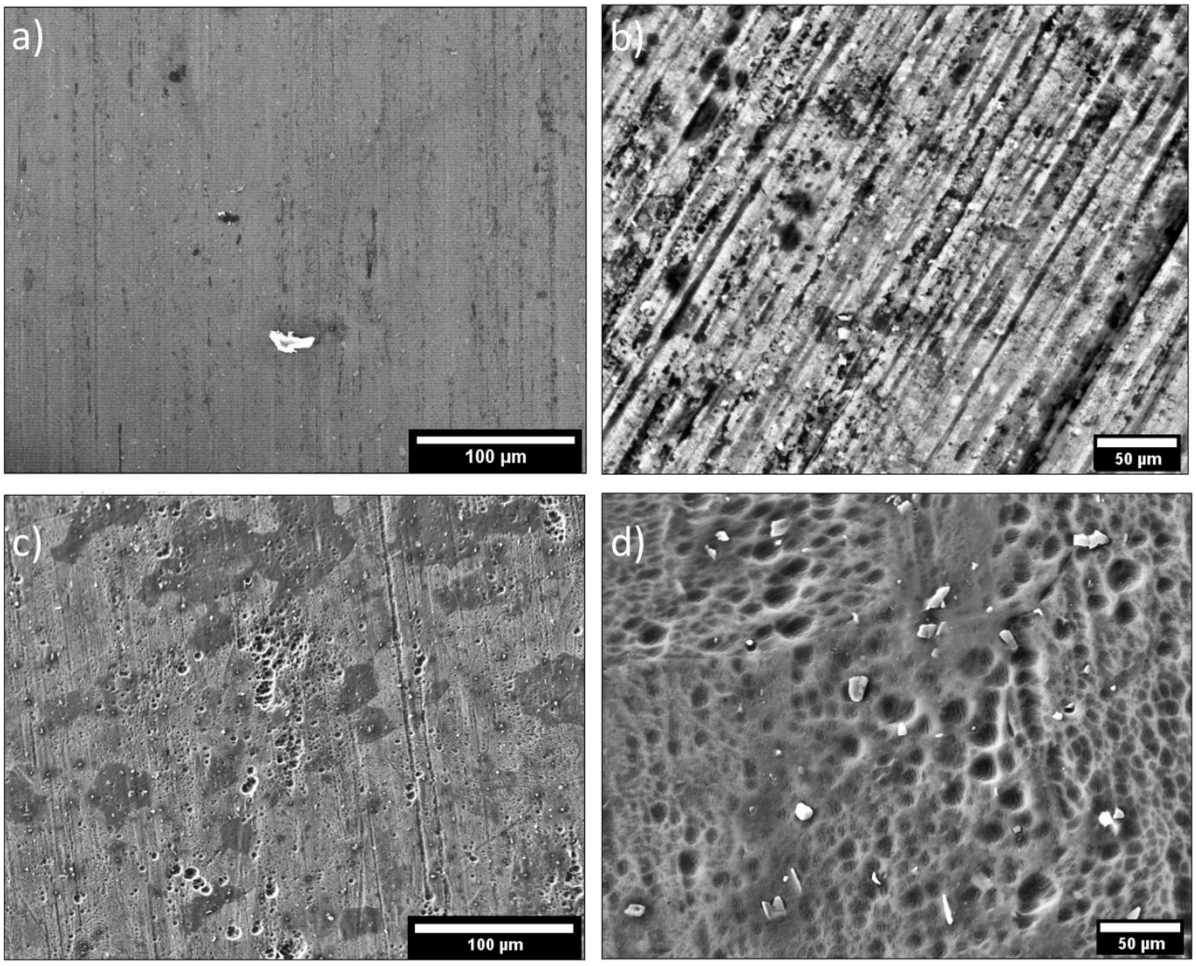

Figure **2**d)[26] revealed after the partial removal of the native Al_2O_3 oxide layer .

In addition, the surface roughness increased after the surface treatment as attested by the formation of holes in

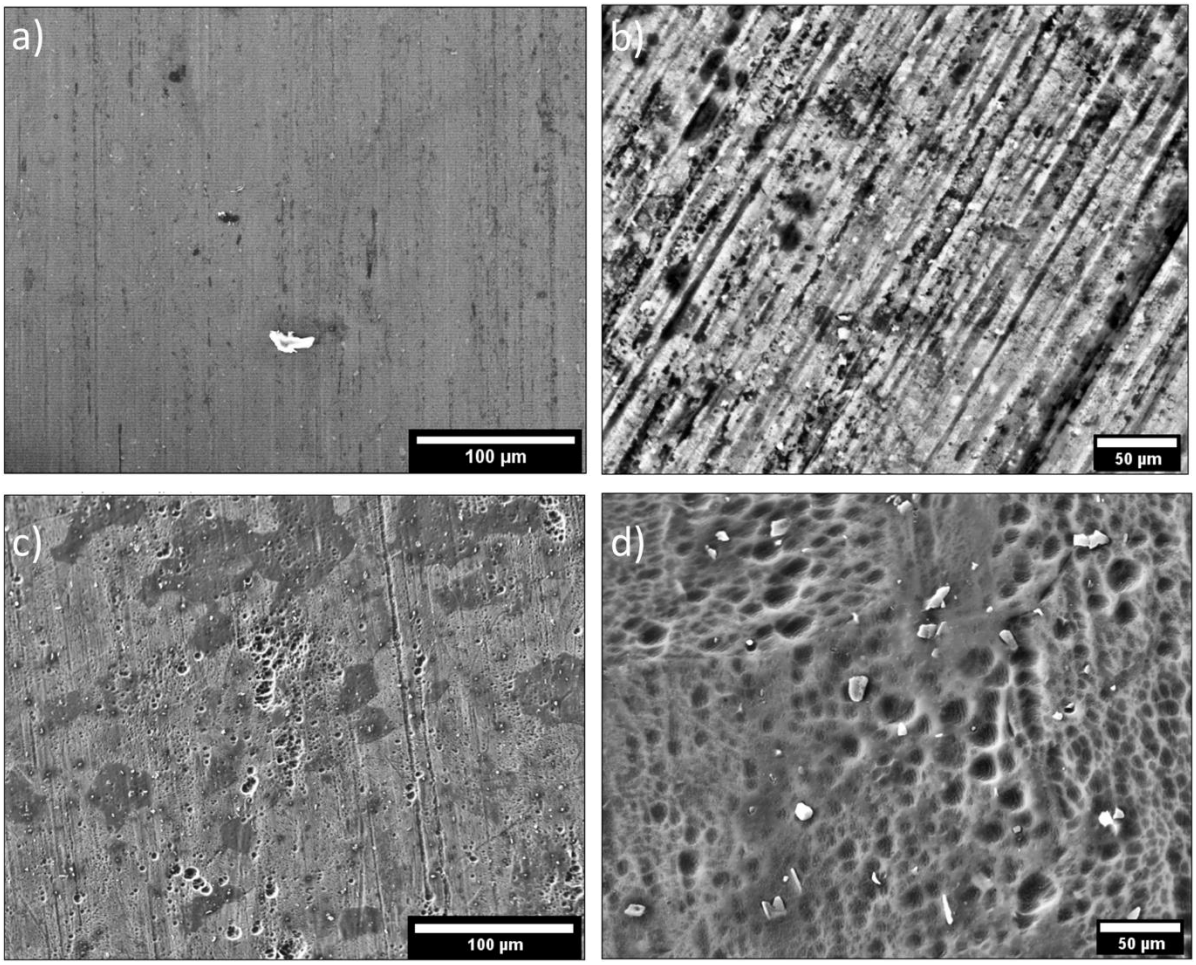

Figure **2**c and Figure 2d. The increasing of the roughness is well-known to promote the adhesion of the coating layer on such type of substrates as reported by Fernández-Hernán, J. P. et al.[27].

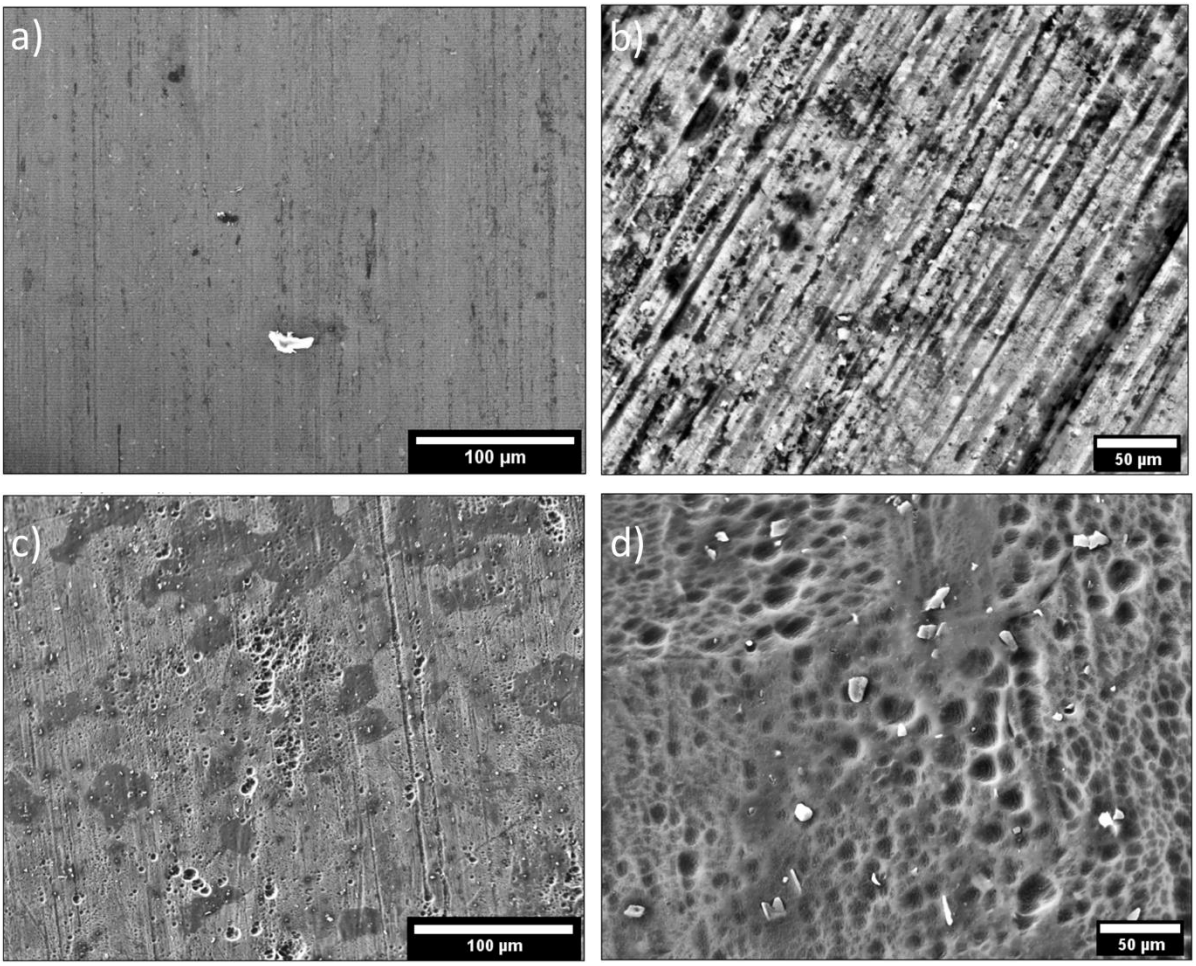

Figure 2. SEM images of Al 2024 substrate: raw material (a and b) and after chemical treatment preparation (c and d).

The XPS investigation of the raw Al 2024 substrate (Figure 3a) showed a small content of aluminum (9 at.% in Table 3) due to the residual organic pollutions (mostly hydrocarbon entities) coming from the machining of the substrate. The Al 2p signal is composed of 3 chemical environments corresponding to Al° at 73.1 eV-73.5 eV, $Al(OH)_3$/AlO(OH) at 74.2 eV and Al_2O_3 at 75.4 eV[28],[29],[30].

Despite the difficulty to observe the metal substrate underneath the natural oxide layer, the presence of Si and Zn traces, as constituent elements of the alloy, can be seen even if they are not

described in the nominal composition given by the provider. These elements are extensively cited in the literature and correspond to the presence of intermetallic particles. The silicon is for instance present in a very small amount into particles such as $MgSi_2$[31],[32].

After the alkaline and the acid treatment, the copper signals (Cu2p3/2 at 933.6 eV and Cu3p3/2 at 77.9 eV) start on emerging from the XPS profile (Figure 3c). The copper enrichment is related to the partial dissolution of the Al_2O_3 layer that exposes minor alloy elements (Al2pAl2O3/ Al2ptotal ratio slightly decreases from 0.83 to 0.70). The complementary calculation of the native oxide layer thickness indicates a decrease from 12.1 nm to 7.2 nm of the Alumina layer after the surface preparation, corroborating the SEM images.

Inversely of what happens to Cu, the Mg and Zn almost completely disappear from the composition, indicating that intermetallic particles like ZnO and $Zn(OH)_2$ were eliminated during surface preparation[33].

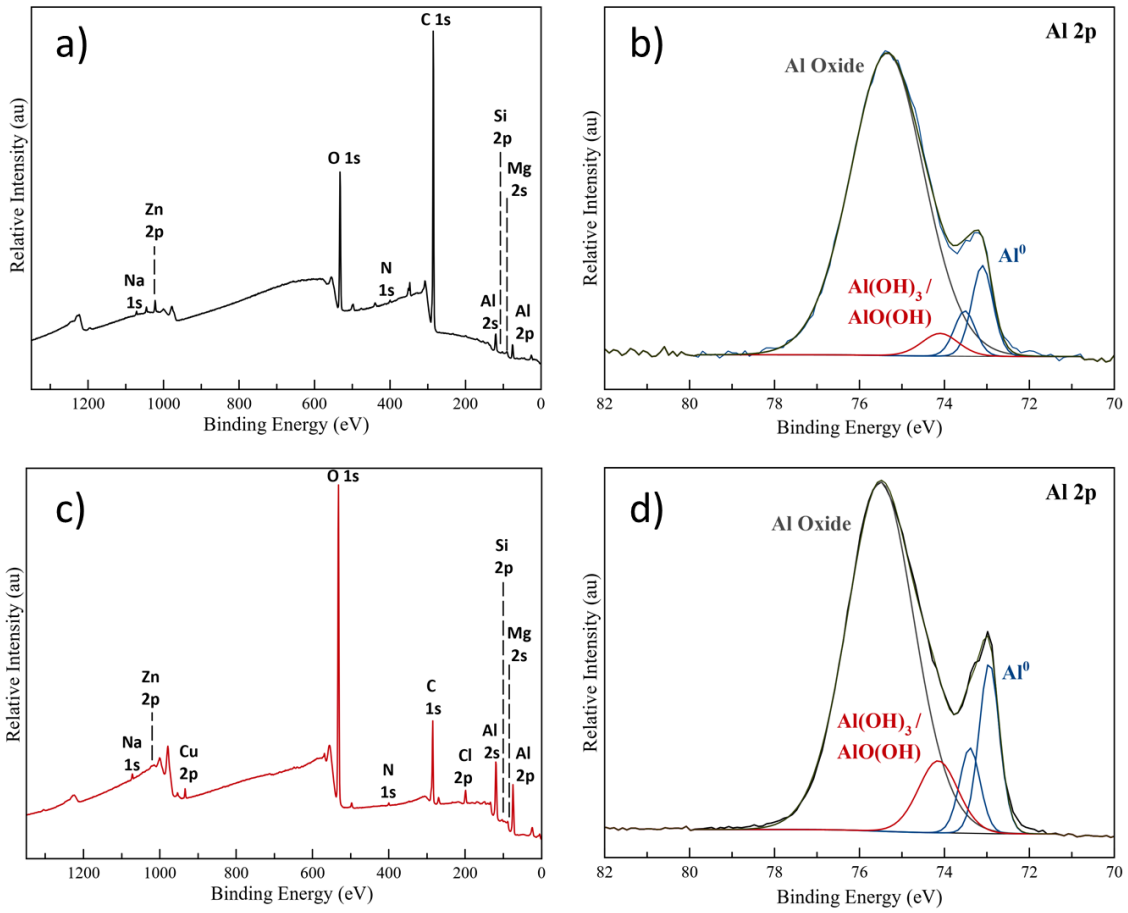

Figure 3. XPS general survey and Al 2p core level spectra of Al 2024 substrate: raw material (a, b) and after chemical treatments (c, d).

In addition, XPS characterization shows an enhancement of the hydroxylation products (twice more important after the chemical cleaning, Table 3) over the surface with the Al 2p component at 74.3 eV growing up (Figure 3d)[34]. This hydroxylation layer increase is supposed to be beneficial for the anchorage and condensation of silica and of the organo-alkoxide TESPSA on the substrate during the pre-functionalization step.

Table 3. XPS quantification of raw Al 2024 and after chemical treatments.

Al 2024 alloy raw	Al 2024 alloy prepared

Core Peak	BE (eV)	at.%	Total At. Conc (%)	BE(eV)	at.%	Total At. Conc (%)
Al 2p	73.1	0.6	9.0	73.0	4.8	35.5
	73.5	0.3		73.5	2.4	
	74.2	0.6		74.3	3.5	
	75.4	7.5		75.4	24.8	
C 1s	285.0	66.0	74.7	285.0	17.8	22.8
	286.3	5.4		286.6	2.9	
	287.9	1.2		288.1	0.5	
	289.1	2.1		289.4	1.6	
O 1s	532.2	14.1	14.1	532.0	38.3	38.3
Mg 2p	51.5	0.7	0.7	-	-	-
Si 2p	102.8	0.4	0.4	104.3	0.9	0.9
Na 1s	1072.0	0.4	0.4	-	-	-
N 1s	399.7	0.4	0.4	400.2	0.5	0.5
Zn 2p	1022.2	0.3	0.3	1022.5	0.1	0.1
Cl 2p	-	-	-	199.1	1.3	1.9
				200.5	0.6	

Hybrid lignin/silica coatings

The Al 2024 substrate was coated with the hybrid lignin/silica layer according to the DR and NDR routes previously described in the experimental section.

Elaboration from the Direct Route (DR)

The SEM image in Figure 4a displays a clearly visible heterogeneous morphology of the coating with holes and also globular particles (zoom in, Figure 4b) that could be assigned to the kraft lignin.

Such heterogeneous structure of the coating was clearly highlighted and confirmed by the XPS characterization. First, the XPS chemical mapping achieved on a 6 mm x 4 mm surface area (Supporting Information – Figure S1) exhibits a non-uniform distribution of the carbon C 1s attributed to the presence of lignin on the surface. A clearly visible hole-like porous structure of the carbon signal can also be observed in Figure S1b. On the other hand, O 1s, Si 2p and Al 2p signals, depicted on the figure S1c, d and e respectively and combined in the overlay Figure S1a, are mostly detected within the holes. The XPS spectra confirm the previous results. The general survey (Figure 5a) exhibits an Al 2p peak (2 at.% - 74.9 eV) attesting of the detection of the substrate. The C 1s spectrum (Figure 5b) is similar to the Kraft lignin one previously shown on Figure 1c with the different carbon components encountered and a total content around 60 at. % (C/O ratio of almost 2.2). Moreover, the XPS Si 2p and O 1s signals (28.8 at.% and 8.3 at.% respectively) are located respectively at 103.0 eV and 532.5 eV that would correspond to a siloxane network. The composition table of the DR Lignin/Silica is present in the Supporting Information (Table S1)[35], [36].

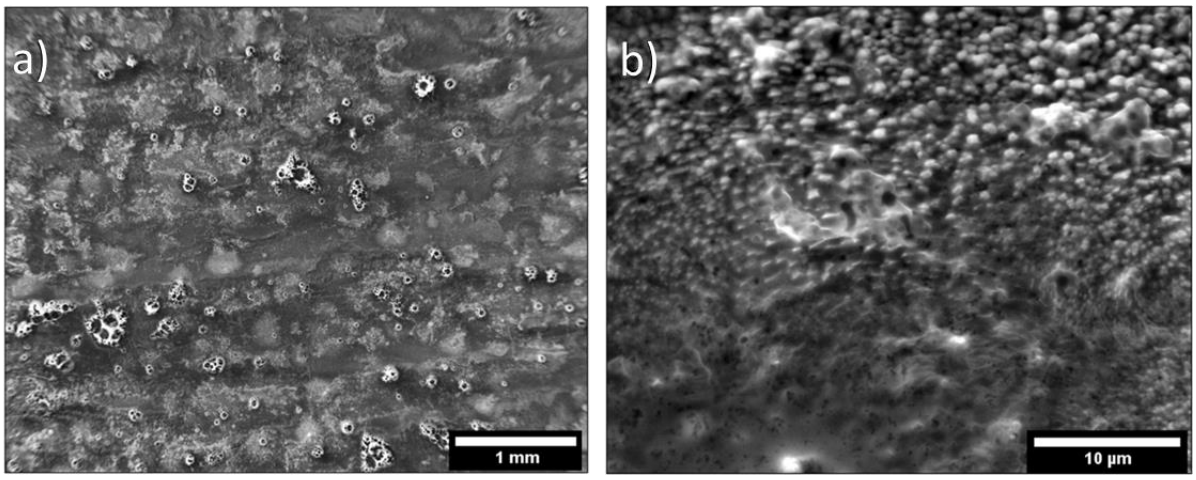

Figure 4. SEM images at low magnification (a) and high magnification (b) of lignin/silica coating on Al 2024 substrate using the DR route.

In this configuration, the probable reason of this heterogeneous structure would come from the nature and the strength of interactions between the hybrid layer and the Al 2024 substrate. Particularly, condensation of silane onto the aluminum substrate can typically occurs through the surface hydroxyl groups. But the strong hydrophobic character of lignin induces probably microphases segregation during the solvent evaporation process leading to a heterogeneous spatial distribution of siloxane bonds onto the aluminum substrate. Such segregation process may also be accentuated by the post deposition thermal treatment of the films.

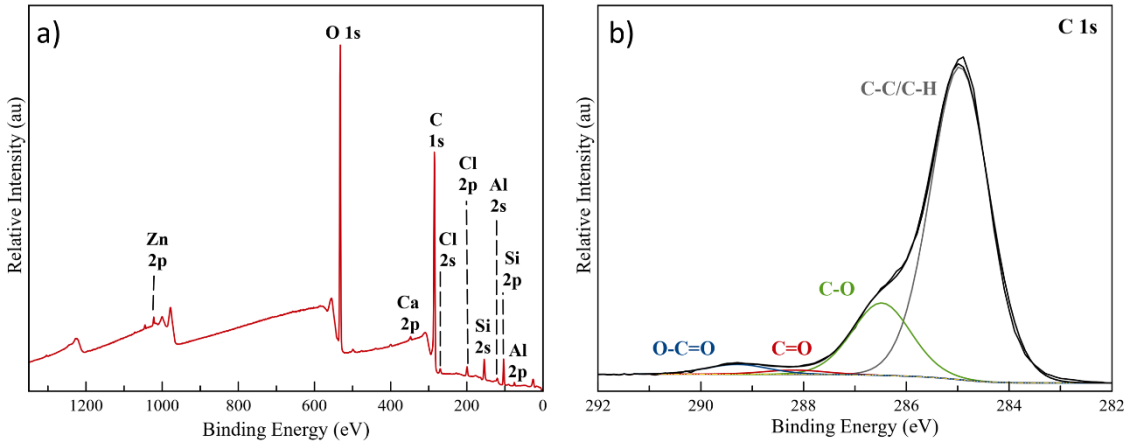

Figure 5. XPS spectra of DR Al 2024 coated substrate: (a) survey spectrum and (b) C 1s core level spectrum.

The FTIR characterization confirms the siloxane-like network, indicating two bands related to the presence of Si that were not visible in lignin spectrum. The first at 950 cm^{-1} could be correlated to Si-O-C=OCH_3 bond and the second one at 1050 cm^{-1} would corresponds to both Si-OR signal and lignin C-H bonds. The bands related to aromatic vibrations (1600 cm^{-1}) and to OH stretching (around 3350 cm^{-1}) are still present in the spectrum, corroborating the presence of lignin[37].

Elaboration from the Non-Direct Route (NDR)

Substrate functionalization

For the NDR route, a surface pre-functionalization with a TESPSA organo-alkoxysilane linker before coating was performed to improve the structuration and the adhesion properties of the hybrid coating layer on the substrates. After the surface modification, the XPS analysis clearly confirmed the change of the surface chemical composition with the appearance of silicon signals (Si 2p at 102.5 eV and Si 2s at 153.4 eV respectively) (Figure 6a). The values of corresponding binding energies attest of the presence of the coupling agent with the detection of $RSiO_3$-Metal chemical environments[38]. The observation of the intense C 1s component at 289.3 eV related to the O-C=O function of the TESPSA (Figure 6b) and the ratio $O_{(O=C)}$/Si at 2.05 confirmed the grafting of the succinic precursor.

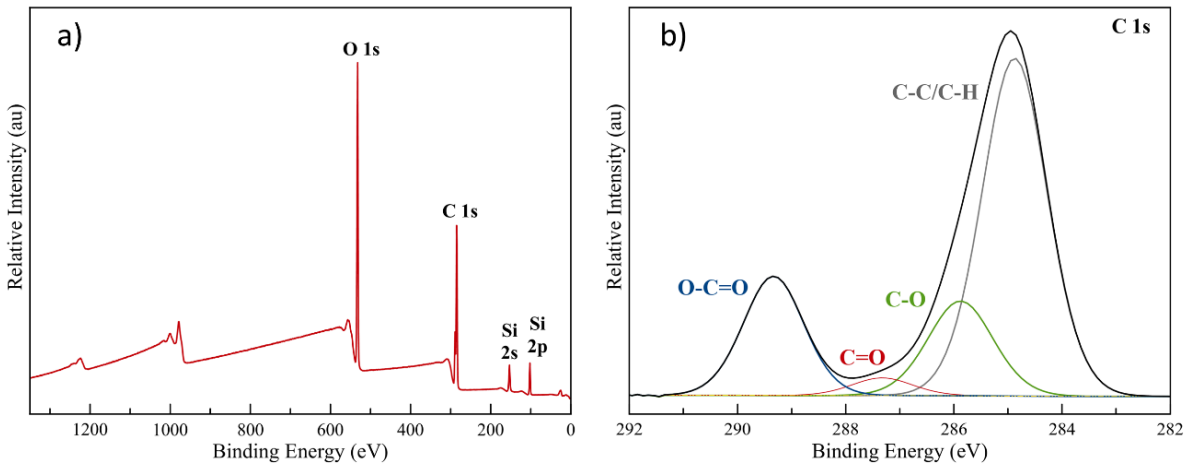

Figure 6. XPS spectra of TESPSA functionalized Al 2024 substrate: (a) survey spectrum and (b) C1s core level spectrum.

Moreover, the absence of Al 2p signal in the XPS survey spectrum reveals that the pre-functionalization layer is thicker than 5 nm due the XPS detection limit depth. Near 60 at.% of

carbon is detected on the surface in comparison to 10 at.% of silicon (Supporting Information – Table S2).

NDR hybrid coating

SEM investigation shows an apparent homogeneous coating in Figure 7a with the presence of a high density of particles or particles aggregates onto the outermost surface. At higher magnification, the Figure 7b displays more details of the coating which appears as a well-interpenetrated like network with some visible small cracks in low amount. Such cracks are commonly reported in the deposition of high thickness hybrid material by dip-coating[39] without affecting, in a large extent, the surface wettability. For comparison, in Figure 7c and 7d are shown coatings that have been prepared in the same conditions without silica source (solution B). The SEM images exhibit a completely different structuration with a low density distribution of isolated or aggregated lignin microparticles.

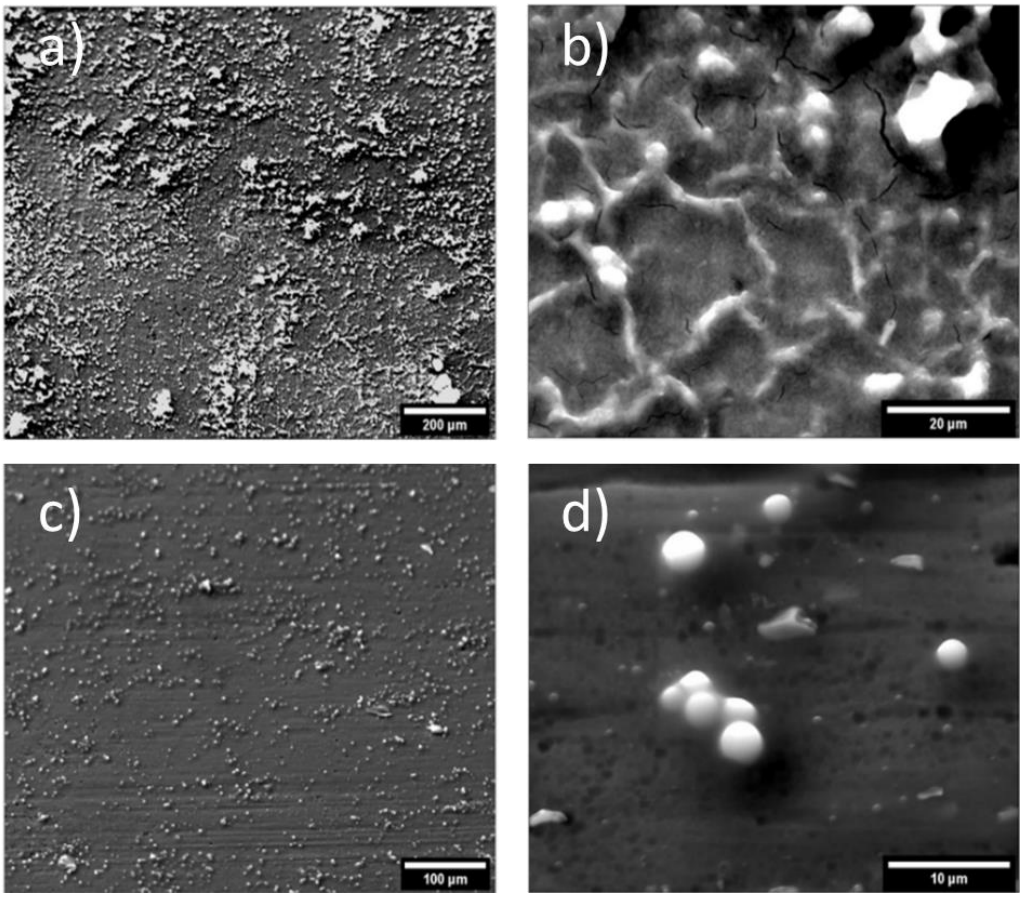

Figure 7. SEM images of hybrid lignin/silica (a, b) or lignin (c, d) coatings on Al 2024 substrate prepared through the NDR route.

To further investigate the chemical properties, FTIR characterization of the hybrid materials layer were performed (Supporting Information – **Erreur ! Source du renvoi introuvable.**2). The results confirmed the presence of the symmetric stretching vibration of the Si-O-Si bonds at 800 cm^{-1}. A large peak is also observable in the 1000-1300 cm^{-1} that is assigned to the overlapping signals of the asymmetric stretching vibrations of Si-O-Si and of the stretching vibrations C-O, C-C and C-H group of lignin. Another remarkable region, that could also be related to the presence of Si, is the intense band at 1700-1750 cm^{-1} that corresponds to the stretching vibrations of C=O coming from undissociated -COOH, -OC–O–Si or -OC-O-C groups[40].

In addition, XPS was performed to study the chemical composition of the materials surface. The general survey (Figure 8a & c) and related quantifications presented in Table 4 shows a substantial increase of carbon content for the NDR hybrid material comparing to the coating prepared with the lignin alone. The quantification also shows a decrease of Si signal from 7.9 at.% to 3.2 at.% for NDR-lignin and NDR Lignin/Silica respectively. Moreover, the C/O ratio of almost 3.8 for NDR Lignin/Silica instead of 3.0 for NDR Lignin is very close to the 3.7 value of Kraft lignin (Table 2) and the C 1s peak profiles (Figure 8d) even match perfectly with the kraft lignin C1s profile showed in Figure 1c . This tends to confirm the presence of Kraft Lignin on the top surface of the coating layer in good agreements with the SEM images in Figure 7c & d.

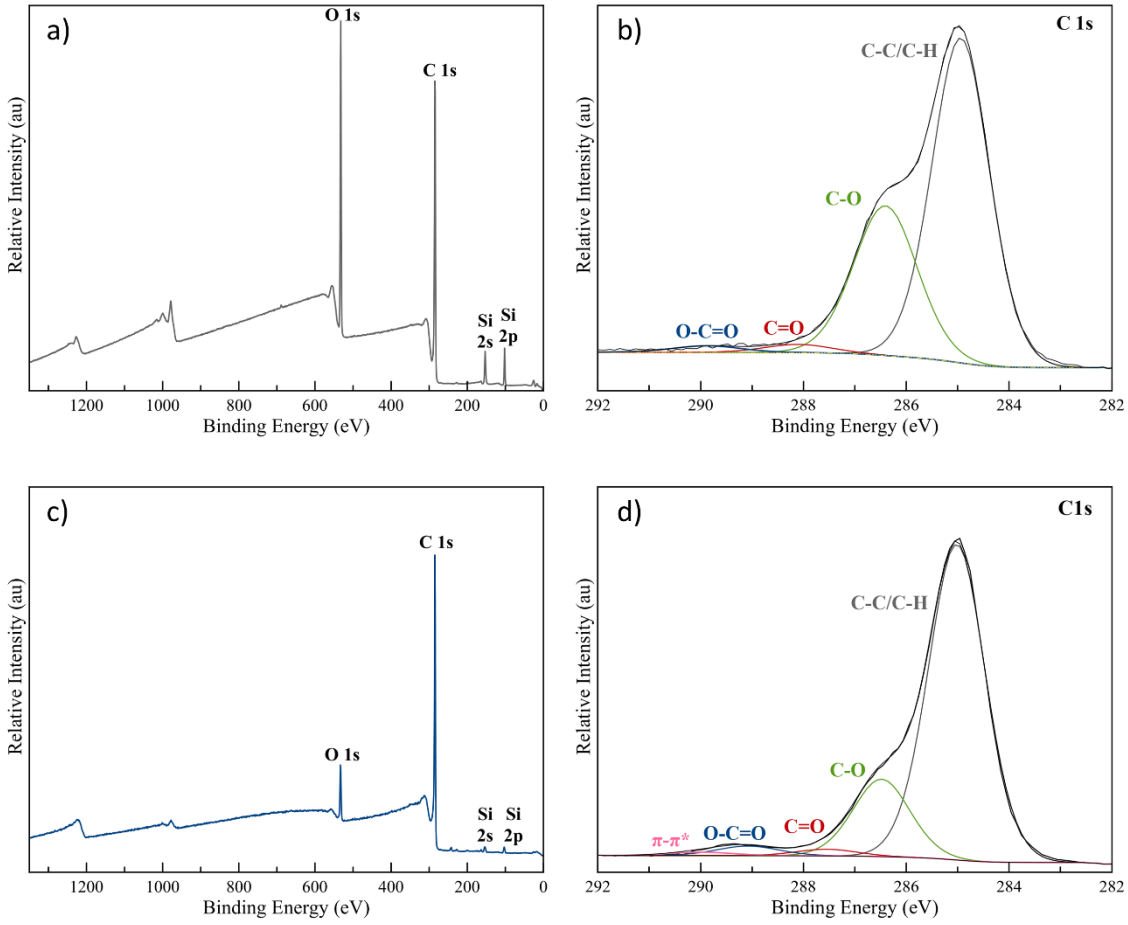

Figure 8. XPS spectra from NDR Al 2024 substrates: a) Survey spectrum of NDR – Lignin coating, b) Carbon 1s core level spectrum of NDR- Lignin coating, c) Survey spectrum of NDR – Lignin/Silica coating and d) Carbon 1s core level spectrum of NDR- Lignin/Silica coating.

The increasing in the lignin particles at the surface of the substrate may be promoted by an esterification process described in the Figure 9. Such process improves the stability of the lignin layer comparing to the DR route and results in the formation of ester bonds coming from the reaction between the –OH groups of the lignin and the carboxylic acid groups of the TESPSA. In addition, the cross-linking of TEOS with TESPSA already demonstrated by Chen, R. et al.[41] has also to be considered. In this case, co-hydrolyzing and co-condensation processes would occur between the silica precursors and the carboxylic acid groups of the succinic linker. Such previous reactions are favored by the use of acid catalyzer and improve the stability of the hybrid coating as well. Those reactions contribute to the generation of a robust interconnected hybrid lignin/silica network as covalent bonds can form to the succinic linker both from the lignin and the silica source. In comparison to the direct route, the stability and the improvement of the lignin deposition is strengthened by the C/Si ratio which increases from 7.6 for DR Lignin/Silica (Supporting Information – Table S1) to 24 for NDR Lignin/Silica. The value of this ratio is only 8.7 for NDR-lignin (Table 4). Such observation tends to conclude to a synergetic effect of the hybridation with TEOS to form a stable hybrid layer.

In addition, the values of the binding energy of Si2p in Table 4 are 102.5 eV and 103 eV for NDR-lignin and NDR-lignin/silica respectively. Considering that for pure SiO2, such the binding energy of Si2p is close to 104 eV[42], we can conclude of a higher number of electronegative atoms close to silicon atoms for NDR lignin and NDR lignin/silica. This is evident for the succinic linker with its non-hydrolysable carbon-silicon bond. For NDR-lignin/silica, the lower value in

comparison to pure SiO2 is characteristic of lignin/silica interactions leading to more carbon rich environments at the vicinity of silicon atoms in the hybrid materials[43],[44].

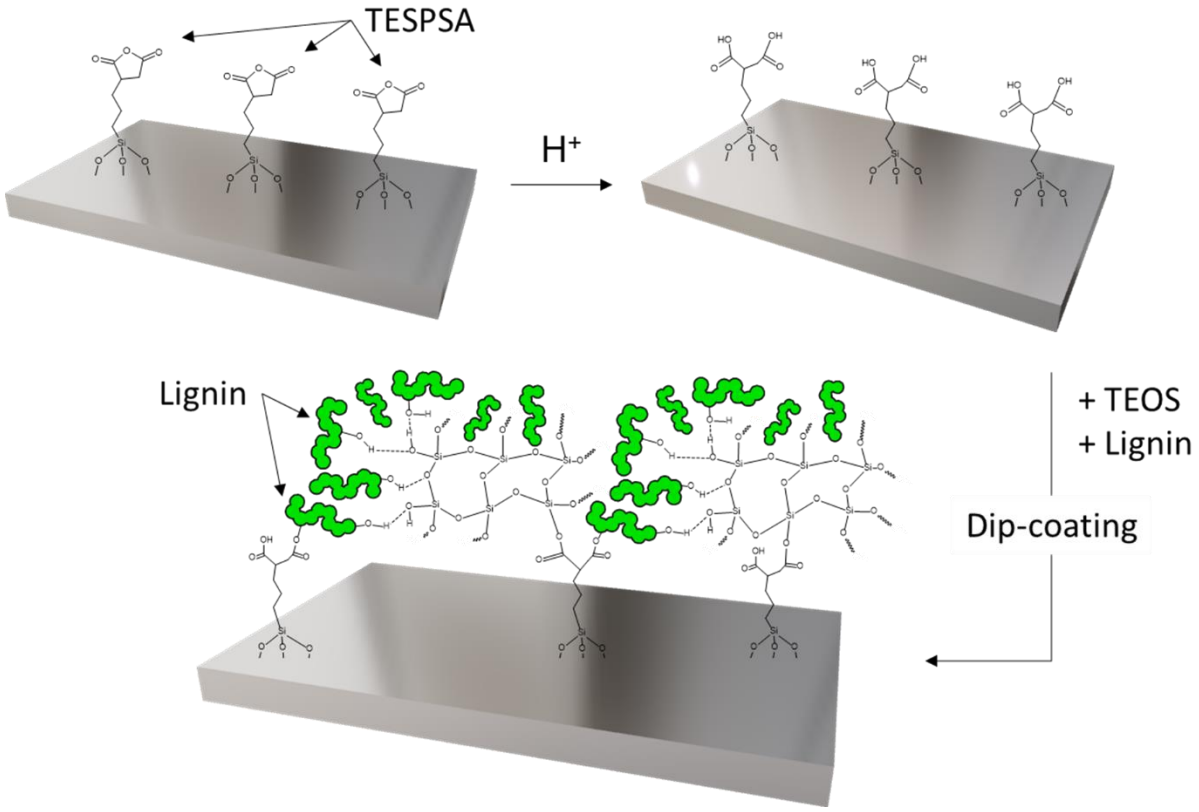

Figure 9. Expected Esterification reaction of between Lignin/Silica hybrid and the TESPSA.

Table 4. XPS quantification analysis of NDR-Lignin and NDR-Lignin/Silica coated samples.

Core Peak	NDR-Lignin			NDR-Lignin/Silica		
	BE (eV)	at.%	Total At. Conc (%)	BE(eV)	at.%	Total At. Conc (%)
C 1s	284.9	47.9	69.3	285.0	58.7	76.7
	286.5	18.9		286.5	14.0	
	287.9	1.7		287.6	1.3	
	289.5	0.8		289.4	2.1	
	-	-		290.2	0.6	

O 1s	533.0	22.8	22.8	532.9	20.1	20.1
Si 2p	102.5	7.9	7.9	103.0	3.1	3.2
C/Si	8.7			24.0		

For a deeper characterization of the hybrid layer structuration, a depth profiling experiment has been performed by etching the surface during 2500 seconds with an Ar^+ ion beam at a 3000 eV energy (Figure 10a and Table **5**5) and was coupled with a systematic XPS experiment (Figure 10a). After 100 sec of etching the Si 2p signal presents the same single component at around 103.0 eV than before etching (Figure 10c), attesting of carbon rich environments in the silica network as already described above and reported elsewhere[45]. When reaching the metal substrate interface after 1000 sec etching, the Al 2p signal of the substrate is visible with the same signature than previously described in section 3.2.1 (Figure 10f).

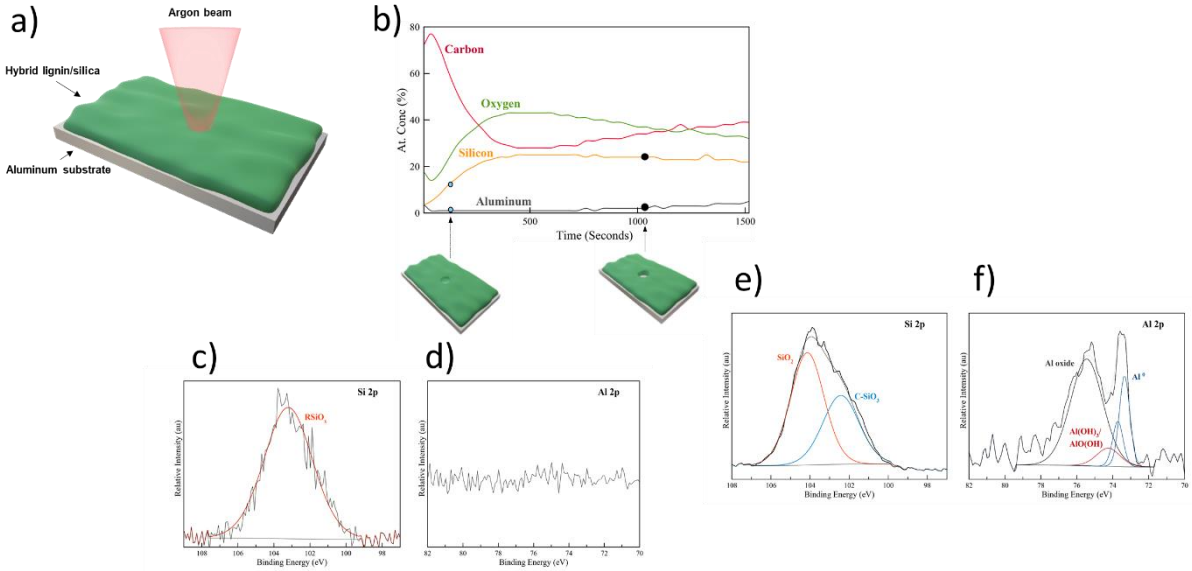

Figure 10. Etching beam of NDR Lignin/Silica coating: (a) graphical representation of the procedure, (b) evolution of the elements concentration (at.%) during the etching process, (c) XPS spectra of Al 2p core level spectrum after 100 sec of Ar^+ etching , (d) Si 2p core level spectrum after 100 sec of Ar^+ etching f ,(e) XPS spectra of Al 2p core level spectrum after 1000 sec of Ar+ etching and (f) Si 2p core level spectrum after 1000 sec of Ar^+ etching .

At this point, the experimental profile of the Si 2p peak splits into two components at 102.4 eV and 104.1 eV respectively (Figure 10e). The first component at low binding energy is associated with the TESPSA layer (Supporting Information - Table S2) while the other one is characteristic of SiO_2[46]. This confirm the location of the substrate/succinic linker interface a 1000s with a SiO_2 network connected to the functionalization layer of TESPA. Such observations are in good agreement with the evolution of the C/Si ratio from 24 to 2.3 (table 5) between 100s and 1000s etching respectively. This confirms a heterogeneous structuration of the coating from the surface to the substrate. Indeed, Lignin tends to segregate at the surface of the coating layer whereas its concentration decreases while approaching the substrate interface. Concomitantly, the contribution of the inorganic part evolves in the opposite way with a higher concentration of silica close to the aluminum substrate.

Table 5. XPS quantification analysis of NDR sample before and after Ar^+ etching.

Core Peak	NDR-Lignin/Silica			NDR-L/S 100 sec etched			NDR-L/S 1000 sec etched		
	BE (eV)	at.%	Total At. Conc (%)	BE (eV)	at.%	Total At. Conc (%)	BE (eV)	at.%	Total At. Conc (%)
Al 2p	-	-	-	-	-	-	73.3	0.6	2.9
	-	-		-	-		73.7	0.3	

	-	-		-	-		74.2	0.3	
	-	-		-	-		75.4	1.7	
	285.0	58.7		284.9	70.7		285.1	41.3	
	286.5	14.1		286.3	12.8		286.4	5.0	
C 1s			76.8			88.6			49.6
	287.6	1.6		287.7	2.2		287.7	2.2	
	289.3	2.4		289.3	2.9		289.3	1.1	
O 1s	532.7	20.0	20.0	533.0	7.3	7.3	533.3	26.0	26.0
	103.0	3.2		103.2	4.1		102.4	12.9	
Si 2p			3.2			4.1			21.5
	-	-		-	-		104.1	8.6	
C/Si	24.0			21.6			2.3		

Wettability Analysis

The Static Water Contact Angle (WCA) experiment demonstrated a direct relation between samples hydrophobicity, expressed by higher angles, and the O/C ratio reduction in relation with a higher content of Lignin at the material surface. Therefore, after Lignin/Silica coating there was a substantial elevation of the contact angles confirming that the effectiveness of the covering layer, as can be seen in Figure 11.

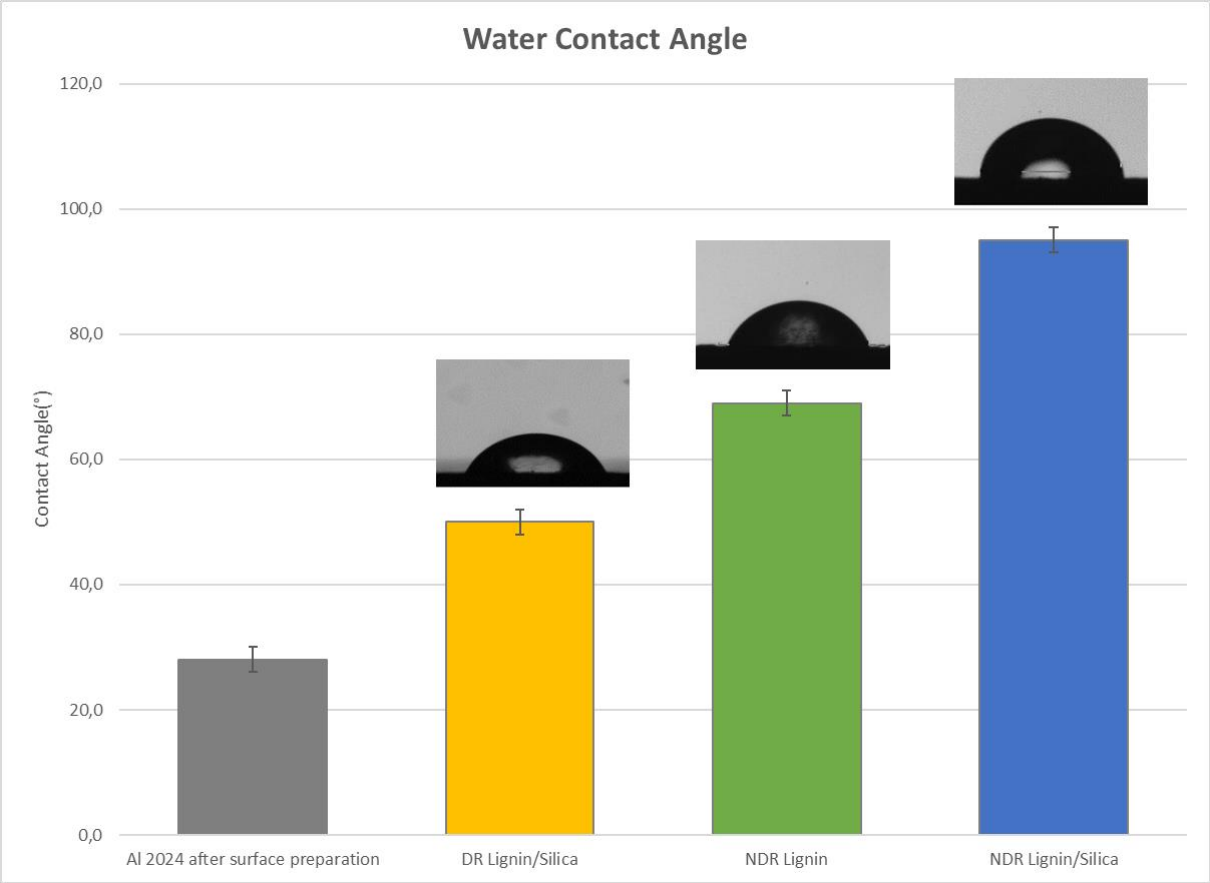

Figure 11. Water Contact Angle of the different studied coated substrates in this work.

The aluminum substrate after preparation presents a very small contact angle of 28° attesting of a hydrophilic character. This result can be explained by the fact that preparation promotes a general hydroxylation of the surface, what increases the affinity with the water. For the coated surfaces, a progressive increase of the contact angle is observed from the DR material to the NDR ones. The substrate covered via DR shows the lowest result of the series with a WCA of 50° and higher values are found for the NDR samples with 69° and 95° for lignin alone and lignin/silica respectively.

Such results are in good agreement with a better stability of the coating and of the higher lignin concentration at the surface of the for the NDR route improving the hydrophobic character of the

material. Such stability can be attributed to the esterification process reducing at the same time the amount of hydroxyl groups promoting the hydrophobicity[47].

The XPS O/C ratio evolution is inversely proportional to the WCA, since the highest ratios were identified in the most hydrophilic samples. The prepared Al 2024 had an O/C ratio of 1.67 indicating a high presence of oxygen on the surface, as expected due to the presence of the hydroxylated products. The O/C ratios of the coated samples ranged from 0.46 for the DR Lignin/Silica to 0.33 for the NDR Lignin and finally 0.26 for the most hydrophobic NDR Lignin/Silica surface.

The improvement of hydrophobic character could also be related to the increased surface roughness of the coated samples, once the Sq value gradually increases from 0.45 μm for Al 2024 after preparation, to 0.63 μm for the DR Lignin/Silica system and finally 1.56 μm for the NDR Lignin/Silica, having a directly proportional relation to the increase of WCA.

As stated by Wang et al.[48] it can be observed that in some heterogeneous samples, where Wenzel's theory can be applied, the increase in roughness will maximize the wettability behavior making hydrophobic surfaces interact even less with water.

Conclusion

In this work, the EISA methodology was coupled with a dip-coating process and was successfully applied to design lignin-silica hybrid films on Al 2024 substrates. In order to control the different steps of the elaboration process and to fully study the interfaces of the hybrid materials, a deep surface characterization methodology by XPS was deployed combined with SEM imaging.

For instance, the microscopic observations revealed the presence of Lignin nanoparticles at the surface of the coating for the NDR route. It is confirmed by the strong percentage increase in the C/Si ratio seen in XPS (approximately 215%) when NDR is compared to DR, that attests of an increased content of lignin at the surface of the coating and of a better stability of the film due to the TESPSA pre-functionalization comparing to the direct route. The evolution of the C/Si at.% ratio and the Si2p binding energy from the outermost surface to the layers close to the substrate indicates an heterogeneous in-depth structuration of the hybrid layer. Indeed, a segregation process of the lignin at the surface of the coating has been observed for the NDR route improving the hydrophobic character of the films with an obtained WCA angle of 95°. Finally, such methodology based on the pre-functionalization step of the substrate combining to the powerful and versatile EISA/dip-coating sol-gel deposition process could be easily adapted to other metal substrates or extended to the development of other bio sourced/silica based hybrid materials for a wide variety of applications.

Supporting Information

XPS chemical map with each element distribution and its combination for the DR – Lignin/Silica sample (PDF)

XPS quantification composition table for the DR – Lignin/Silica and for the pre-functionalized substrate (PDF)

FTIR spectrum for the NDR – Lignin/Silica sample with each band attribution

Author Information

Corresponding Author

Jean-Charles Dupin - Université de Pau et Pays de l'Adour, E2S UPPA, IPREM/CNRS, UMR5254, 64000, Pau, France ; Email : dupin@univ-pau.fr

Author Contributions

The manuscript was written through contributions of all authors. All authors have given approval to the final version of the manuscript.

Notes

The authors declare no competing financial interest.

Acknowledgments

The authors are extremely grateful to I-Site E2S Program "Advanced R&D Solutions for Energy & the Environment" funding from the UPPA - Inria - INRAe - CNRS research consortium.

References

[1]. Sankaran, K. K.; Mishra, R. S. Chapter 4 - Aluminum Alloys; Sankaran, K. K., Mishra, R. S. B. T.-M. and D. of A. with H. M., Eds.; Elsevier, 2017; pp 57–176. https://doi.org/https://doi.org/10.1016/B978-0-12-812068-2.00004-7

[2]. Carreira, A. F.; Pereira, A. M.; Vaz, E. P.; Cabral, A. M.; Ghidini, T.; Pigliaru, L.; Rohr, T. Alternative Corrosion Protection Pretreatments for Aluminum Alloys. J. Coatings Technol. Res. 2017, 14 (4), 879–892. https://doi.org/10.1007/s11998-017-9922-9

[3]. Stoica, A. I.; Światowska, J.; Romaine, A.; Di Franco, F.; Qi, J.; Mercier, D.; Seyeux, A.; Zanna, S.; Marcus, P. Influence of Post-Treatment Time of Trivalent Chromium Protection Coating on Aluminium Alloy 2024-T3 on Improved Corrosion Resistance. Surf. Coatings Technol. 2019, 369, 186–197. https://doi.org/10.1016/j.surfcoat.2019.04.051

[4]. Coquery, C.; Carosio, F.; Negrell, C.; Caussé, N.; Pébère, N.; David, G. New Bio-Based Phosphorylated Chitosan/Alginate Protective Coatings on Aluminum Alloy Obtained by the LbL Technique. Surfaces and Interfaces 2019, 16, 59–66. https://doi.org/10.1016/j.surfin.2019.04.010.

[5]. Dastpak, A.; Yliniemi, K.; Monteiro, M. C. de O.; Höhn, S.; Virtanen, S.; Lundström, M.; Wilson, B. P. From Waste to Valuable Resource: Lignin as a Sustainable Anti-Corrosion Coating. Coatings 2018, 8 (12). https://doi.org/10.3390/COATINGS8120454.

[6]. Dastpak, A.; Ansell, P.; Searle, J. R.; Lundström, M.; Wilson, B. P. Biopolymeric Anticorrosion Coatings from Cellulose Nanofibrils and Colloidal Lignin Particles. ACS Appl. Mater. Interfaces 2021, 13 (34), 41034–41045. https://doi.org/10.1021/ACSAMI.1C08274/SUPPL_FILE/AM1C08274_SI_001.PDF.

[7]. Vanholme, R.; Demedts, B.; Morreel, K.; Ralph, J.; Boerjan, W. Lignin Biosynthesis and Structure. Plant Physiol. 2010, 153 (3), 895–905. https://doi.org/10.1104/pp.110.155119.0).

[8]. Liu, Q.; Luo, L.; Zheng, L. Lignins: Biosynthesis and Biological Functions in Plants. Int. J. Mol. Sci. 2018, 19 (2). https://doi.org/10.3390/ijms19020335.

[9]. Mandlekar, N.; Cayla, A.; Rault, F.; Giraud, S.; Salaün, F.; Malucelli, G.; Guan, J.-P. An Overview on the Use of Lignin and Its Derivatives in Fire Retardant Polymer Systems. Lignin - Trends Appl. 2018. https://doi.org/10.5772/intechopen.72963.

[10]. Demuner, I. F.; Colodette, J. L.; Demuner, A. J.; Jardim, C. M. Biorefinery Review: Wide-Reaching Products through Kraft Lignin. BioResources 2019, 14 (3), 7543–7581. https://doi.org/10.15376/biores.14.3.demuner.

[11]. Kraft Lignin Market Research Report by Application (Binders And Resins, Pesticides And Fertilizers, and Thermoplastic Polymers), by Region (Americas, Asia-Pacific, and Europe, Middle East & Africa) - Global Forecast to 2026 - Cumulative Impact of COVID-19 https://www.researchandmarkets.com/reports/4905005/kraft-lignin-market-research-report-by

[12]. Gillet, S.; Aguedo, M.; Petitjean, L.; Morais, A. R. C.; Da Costa Lopes, A. M.; Łukasik, R. M.; Anastas, P. T. Lignin Transformations for High Value Applications: Towards Targeted Modifications Using Green Chemistry. Green Chem. 2017, 19 (18), 4200–4233. https://doi.org/10.1039/c7gc01479a.

[13]. S.B. Lee, P. Luner, The wetting and interfacial properties of lignin, Tappi J. 55 (1), 1972, 16–21

[14]. Alwadani, N.; Ghavidel, N.; Fatehi, P. Surface and Interface Characteristics of Hydrophobic Lignin Derivatives in Solvents and Films. Colloids Surfaces A Physicochem. Eng. Asp. 2021, 609 (October 2020), 125656. https://doi.org/10.1016/j.colsurfa.2020.125656.

[15]. Eraković, S.; Janković, A.; Veljović, D.; Palcevskis, E.; Mitrić, M.; Stevanović, T.; Janaćković, D.; Miskovic-Stankovic, V. Corrosion Stability and Bioactivity in Simulated Body Fluid of Silver/Hydroxyapatite and Silver/Hydroxyapatite/Lignin Coatings on Titanium Obtained by Electrophoretic Deposition. J. Phys. Chem. B 2013, 117 (6), 1633–1643. https://doi.org/10.1021/jp305252a.

[16]. Li, J.; Wang, M.; She, D.; Zhao, Y. Structural Functionalization of Industrial Softwood Kraft Lignin for Simple Dip-Coating of Urea as Highly Efficient Nitrogen Fertilizer. Ind. Crops Prod. 2017, 109 (July), 255–265. https://doi.org/10.1016/j.indcrop.2017.08.011.

[17]. Sanchez, C.; Rozes, L.; Ribot, F.; Laberty-Robert, C.; Grosso, D.; Sassoye, C.; Boissiere, C.; Nicole, L. "Chimie Douce": A Land of Opportunities for the Designed Construction of Functional Inorganic and Hybrid Organic-Inorganic Nanomaterials. Comptes Rendus Chim. 2010, 13 (1–2), 3–39. https://doi.org/10.1016/j.crci.2009.06.001.

[18]. Grosso, D. How to Exploit the Full Potential of the Dip-Coating Process to Better Control Film Formation. J. Mater. Chem. 2011, 21 (43), 17033–17038. https://doi.org/10.1039/c1jm12837j.

[19]. Wei, J.; Wang, H.; Deng, Y.; Sun, Z.; Shi, L.; Tu, B.; Luqman, M.; Zhao, D. Solvent Evaporation Induced Aggregating Assembly Approach to Three-Dimensional Ordered Mesoporous Silica with Ultralarge Accessible Mesopores. J. Am. Chem. Soc. 2011, 133 (50), 20369–20377. https://doi.org/10.1021/ja207525e.

[20]. MB, I.; NC, P. A Comparative Study on Surface Treatments in the Immobilization Improvement of Hexahistidine-Tagged Protein on the Indium Tin Oxide Surface. J. Nanomed. Nanotechnol. 2016, 07 (02). https://doi.org/10.4172/2157-7439.1000372.

[21]. Faustini, M.; Louis, B.; Albouy, P. A.; Kuemmel, M.; Grosso, D. Preparation of Sol-Gel Films by Dip-Coating in Extreme Conditions. J. Phys. Chem. C 2010, 114 (17), 7637–7645. https://doi.org/10.1021/jp9114755.

[22]. Alexander, M. R.; Thompson, G. E.; Zhou, X.; Beamson, G.; Fairley, N. Quantification of Oxide Film Thickness at the Surface of Aluminium Using XPS. Surf. Interface Anal. 2002, 34 (1), 485–489. https://doi.org/10.1002/sia.1344.

[23]. Flores-Mancera, M. A.; Villarrubia, J. S.; Massillon-Jl, G. Electron Inelastic Mean Free Paths for LiF, CaF2, Al2O3, and Liquid Water from 433 KeV down to the Energy Gap. ACS Omega 2020, 5 (8), 4139–4147. https://doi.org/10.1021/acsomega.9b03872.

[24]. Brazil, T. R.; Costa, R. N.; Massi, M.; Rezende, M. C. Structural, Morphological, and Thermal Characterization of Kraft Lignin and Its Charcoals Obtained at Different Heating Rates. Materials Research Express 2018, 5 (4), 45502. https://doi.org/10.1088/2053-1591/aab7c2.

[25]. Nada, A. A. M. A.; El-Sakhawy, M.; Kamel, S. M. Infra-Red Spectroscopic Study of Lignins. Polymer Degradation and Stability 1998, 60 (2–3), 247–251. https://doi.org/10.1016/s0141-3910(97)00072-4.

[26]. DeRose, J. A.; Bałkowiec, A.; Michalski, J.; Suter, T.; Kurzydlowski, K. J.; Schmutz, P. Microscopic and Macroscopic Characterisation of an Aerospace Aluminium Alloy (AA2024). 2012, 6, 23–38. https://doi.org/10.2495/978-1-84564-752-0/03.

[27]. Fernández-Hernán, J. P.; López, A. J.; Torres, B.; Rams, J. Influence of Roughness and Grinding Direction on the Thickness and Adhesion of Sol-Gel Coatings Deposited by

Dip-Coating on AZ31 Magnesium Substrates. A Landau–Levich Equation Revision. Surf. Coatings Technol. 2021, 408, 126798. https://doi.org/https://doi.org/10.1016/j.surfcoat.2020.126798.

[28]. Reddy N.; Bera, P.; Reddy, V. R.; Sridhara, N.; Dey, A.; Anandan, C.; Sharma, A. K. XPS Study of Sputtered Alumina Thin Films. Ceramics International 2014, 40 (7 PART B), 11099–11107. https://doi.org/10.1016/j.ceramint.2014.03.133.

[29]. Zähr, J.; Oswald, S.; Türpe, M.; Ullrich, H. J.; Füssel, U. Characterisation of Oxide and Hydroxide Layers on Technical Aluminum Materials Using XPS. In Vacuum; 2012; Vol. 86, pp 1216–1219. https://doi.org/10.1016/j.vacuum.2011.04.004.

[30]. Rotole, J. A.; Sherwood, P. M. A. Gamma-Alumina (γ-Al2O3) by XPS. Surface Science Spectra 1998, 5 (1), 18–24. https://doi.org/10.1116/1.1247852.

[31]. Hahn, G. T.; Rosenfield, A. R. Metallurgical Factors Affecting Fracture Toughness of Aluminum Alloys. Metall. Trans. A 1975, 6 (3), 653–668. https://doi.org/10.1007/BF02672285.

[32]. Hughes, A. E.; Boag, A.; Glenn, A. M.; McCulloch, D.; Muster, T. H.; Ryan, C.; Luo, C.; Zhou, X.; Thompson, G. E. Corrosion of AA2024-T3 Part II: Co-Operative Corrosion. Corros. Sci. 2011, 53 (1), 27–39. https://doi.org/10.1016/j.corsci.2010.09.030.

[33]. Nelson, K. J. H.; Hughes, A. E.; Taylor, R. J.; Hinton, B. R. W.; Wilson, L.; Henderson, M. Characterisation of Aluminium Alloys after HNO3/HF–NaOH–HNO3/HF

Pretreatment. Mater. Sci. Technol. 2001, 17 (10), 1211–1221. https://doi.org/10.1179/026708301101509287.

[34]. Kameshima, Y.; Yasumori, A.; Okada, K. XPS and X-ray AES (XAES) Study of Various Aluminate Compounds. Hyomen Kagaku. 2000, 21(8),481-487

[35]. Ouyang, M.; Yuan, C.; Muisener, R. J.; Boulares, A.; Koberstein, J. T. Conversion of Some Siloxane Polymers to Silicon Oxide by UV/Ozone Photochemical Processes. Chemistry of Materials 2000, 12 (6), 1591–1596. https://doi.org/10.1021/cm990770d.

[36]. Fu, Y.; Ni, Q. Q.; Iwamoto, M. Interaction of PMMA-Silica in PMMA-Silica Hybrids under Acid Catalyst and Catalyst-Less Conditions. Journal of Non-Crystalline Solids 2005, 351 (8–9), 760–765. https://doi.org/10.1016/j.jnoncrysol.2005.01.052.

[37]. Launer, P.; Arkles, B. Infrared Analysis of Organosilicon Compounds; 2013; pp 175–178.

[38]. Aynard, A.; Pessoni, L.; Billon, L. Directed self-assembly in “breath figure” templating of block copolymers followed by soft hydrolysis-condensation: One step towards synthetic bio-inspired silica diatoms exoskeleton. Polymer, 2020, 210, 123047. https://doi.org/10.1016/j.polymer.2020.123047

[39]. Chen, Z.; Burtovyy, R.; Kornev, K. G.; Luzinov, I.; Peng, F. Dense and Crack-Free Mullite Films Obtained from a Hybrid Sol-Gel/Dip-Coating Approach. J. Mater. Res. 2017, 32 (9), 1665–1673. https://doi.org/10.1557/jmr.2017.122.

[40]. Zhang, R.; Xiao, X.; Tai, Q.; Huang, H.; Yang, J.; Hu, Y. Preparation of Lignin-Silica Hybrids and Its Application in Intumescent Flame-Retardant Poly(Lactic Acid) System.

High Performance Polymers 2012, 24 (8), 738–746. https://doi.org/10.1177/0954008312451476.

[41]. Chen, R.; Qu, H.; Guo, S.; Ducheyne, P. The Design and Synthesis of a Soluble Composite Silica Xerogel and the Short-Time Release of Proteins. J. Mater. Chem. B 2015, 3 (16), 3141–3149.

[42]. Paparazzo, E.; Fanfoni, M.; Severini, E. Studies on the Structure of the SiOx/SiO2 Interface. Appl. Surf. Sci. 1992, 56–58, 866–872. https://doi.org/https://doi.org/10.1016/0169-4332(92)90352-X.

[43]. Carlos De Haro, J.; Magagnin, L.; Turri, S.; Griffini, G. Lignin-Based Anticorrosion Coatings for the Protection of Aluminum Surfaces. ACS Sustain. Chem. Eng. 2019, 7 (6), 6213–6222. https://doi.org/10.1021/acssuschemeng.8b06568

[44]. An, L.; Si, C.; Bae, J. H.; Jeong, H.; Kim, Y. S. One-Step Silanization and Amination of Lignin and Its Adsorption of Congo Red and Cu(II) Ions in Aqueous Solution. Int. J. Biol. Macromol. 2020, 159, 222–230. https://doi.org/10.1016/j.ijbiomac.2020.05.072.

[45]. dos Santos, F. C.; Harb, S. v.; Menu, M. J.; Turq, V.; Pulcinelli, S. H.; Santilli, C. v.; Hammer, P. On the Structure of High Performance Anticorrosive PMMA-Siloxane-Silica Hybrid Coatings. RSC Advances 2015, 5 (129), 106754–106763. https://doi.org/10.1039/c5ra20885h.

[46]. Wagner, C. D. NIST X-Ray Photoelectron Spectrometry Database. NIST Stand. Ref. Database 20, Version 4.1 1991, 1–76.

[47]. Hua, Q.; Liu, L.-Y.; Karaaslan, M. A.; Renneckar, S. Aqueous Dispersions of Esterified Lignin Particles for Hydrophobic Coatings. Front. Chem. 2019, 7, 515. https://doi.org/10.3389/fchem.2019.00515.

[48]. Wang, J.; Wu, Y.; Cao, Y.; Li, G.; Liao, Y. Influence of Surface Roughness on Contact Angle Hysteresis and Spreading Work. Colloid and Polymer Science 2020, 298 (8), 1107–1112. https://doi.org/10.1007/s00396-020-04680-x.